Rolling Element Bearing Fault Modelling to Develop a Diagnosis Scheme for Oscillating and Non-uniform Shaft Rotation

Chintamani Mishra *Goutam Chakraborty* *Arun Kumar Samantaray*
Department of Mechanical Engineering, IIT,Kharagpur, India
call2chintu@gmail.com goutam@mech.iitkgp.ernet.in samantaray@mech.iitkgp.ernet.in

***Abstract*— Rolling element bearings are widely used in rotating machines and their faults can lead to excessive vibration levels and/or complete seizure of the machine. Under special operating conditions such as oscillating rotor motion or full rotations with non-uniform speed, the available fault diagnosis methods cannot be applied for bearing fault diagnosis. Further to that, fault symptoms in some machines which operate at very slow speed in the range of fractional rpm cannot be extracted through usual measurement and signal processing techniques. Typical examples are LD furnace, heavy rolling mill, *etc*.**

In extremely slow speed or variable speed operation, rolling element slip becomes predominant. In this article, we present a bond graph model of the rolling element bearing by taking into account the nonlinear contact stiffness, contact friction, cage dynamics, rolling element pre-compression and localized faults. The rotor is supposed to be either velocity or torque driven where the external load decides the rotor speed.

Simulation of the bond graph model developed here yields the vibration signatures corresponding to specific fault or combinations thereof. The simulation model outputs are used to fine-tune diagnosis scheme which consists of two post-processing steps. The vibration signature is concurrently acquired with the instantaneous angular velocity or position. For oscillating motion, we use a simple potentiometer with appropriate engagement with the rotor shaft. In the first step of post-processing, it is assumed that when a fault is encountered, impact leads to ringing the bearing natural frequencies. Thus, the generated time-domain vibration signal is filtered through a band-pass filter whose pass-band contains the bearing natural frequency. In the second phase, the vibration signature as a time-series data is converted to a dataset of vibration amplitude versus the angular position. The 360 degree angular position range is then segmented into small steps of 1 to 5 degree bands. The averaged vibration amplitudes at various angular position bands are then plotted in the form of a histogram. The features of this histogram are then compared to bearing characteristic angles (mapped form of bearing characteristic frequencies to eliminate explicit dependence on time or frequency) to isolate the faults.

Keywords*— *Rolling element bearing; Machinery fault diagnosis; Bond graph; Signal processing.

I. INTRODUCTION

Faults which typically occur in rolling element bearings are usually due to localized defects in the outer-race, inner-race, the roller, or the cage. Such defects generate series of impacts every time these defects come in contact with the mating surfaces. These impulses excite the entire system including the bearing, the sensor and the structure where the bearing is mounted. Through different signal processing techniques, the bearing characteristic frequencies (BCF) can be identified from vibration signals. There is abundant literature on diagnosis of rolling element faults through vibration analysis [1]. Several signal processing steps may be used to extract the relevant features from the acquired measurements before the diagnosis scheme can be applied [2]. There are different techniques in time and frequency domain such as high-frequency resonance (HFR) [3-5], spectral kurtosis [6], minimum entropy de-convolution [7], Teager energy operator (TEO) [8, 9], higher order spectral analysis [10], shock pulse and spike energy analysis [11-12], etc. which are generally used for diagnosis of faults in rolling element bearings under different operating conditions. In time frequency domain, techniques like Hilbert transform and wavelet transform are widely used in diagnosis of rolling element bearing faults [13-15].

In laboratory scale, one may introduce deliberate bearing faults and then take corresponding measurements from the machine operating with the faulty bearing. Such fault simulator systems are commercially available for laboratory use. However, it is usually impossible to build a database of bearing fault signatures for industrial machines. It may take years for a good bearing to develop any kind of fault. Therefore, a model of the machine with bearings can be used to generate a rich database of measurements with variety of faults in bearings and other machine components [16, 17]. Moreover, a model is scalable and any number of faults can be introduced in it. A model-based scheme to build up a fault monitoring system is an economical solution.

In dynamic modeling of rolling element bearings, lot of work has been reported: quasi-static modeling in [18], generalized equation of motion in [19, 20], multi-body dynamics model in [21, 22], and defect geometry modeling and evolution in [23, 24].

II. BALL BEARING KINEMATICS

The kinematic modelling requires only bearing geometry parameters. These are the diameter of ball d, pitch diameter D, frequency of outer race rotation f_O, frequency of inner race rotation f_i, number of balls N, and contact angle ψ (Fig. 1). General expression for ball

pass frequency for inner race (BPFI), ball pass frequency of outer race (BPFO) and ball spin frequency (BSF) are,

$$f_{\text{BPFI}} = N\left(f_o - f_i\right)\left(1 + d/D\cos(\psi)\right)/2 \quad (1)$$

$$f_{\text{BPFO}} = N\left(f_o - f_i\right)\left(1 - d/D\cos(\psi)\right)/2 \quad (2)$$

$$f_{\text{BSF}} = \frac{D\left(f_o - f_i\right)}{2d}\left(1 - \left(\frac{d}{D}\cos(\psi)\right)^2\right) \quad (3)$$

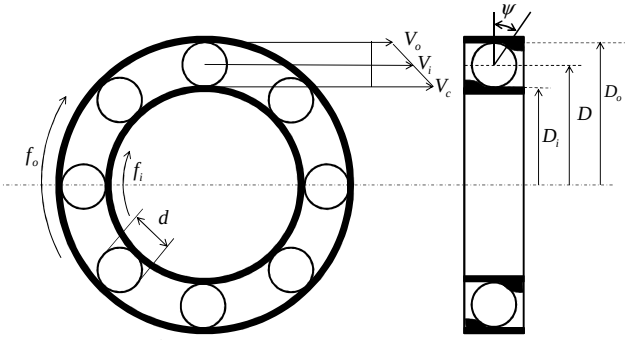

Fig.1. Geometry of rolling element bearing.

III. Dynamic Modelling of Rolling Element Bearing

It is difficult to formulate equations of motion of different parts of rolling element bearings and evaluate their performance under extreme conditions such as very low speed, very high speed, and in presence of fault in any element. However, some simplification of kinetics based on engineering approximations can be employed to generate a sufficiently accurate model.

A rolling element bearing consists of rolling element, inner race, outer race and cage as its principal parts. Interaction of many factors determines the rolling element bearing's dynamic characteristics. In this article, the system is modeled as a multi-body system. Rolling element bearing frictional force is a function of speed, contact deformation, contact angle and inertial loading. We have included nonlinear contact stiffness, contact slip, traction between elements, drive torque, cage dynamics, pre-compression and localized faults in the model. The effects due to axial movement and lubrication are neglected. The developed multi-body dynamics model of the deep-groove ball bearing/roller bearings considers planar motion of the rolling elements. Thus, each rolling element has three degrees of freedom. Likewise, the inner race, outer race and the cage have three degrees of freedom each. The rolling elements are constrained to move within the cage. The cage center, inner race center and outer race centers are at different locations as decided by the dynamics of the system. The instantaneous locations of these centers are used to compute the contact points of the rolling elements with the races. Faults in the outer race, inner race and the rolling elements have been modeled as small notches. The contact between all the mating surfaces is considered as surface contact.

A. Contact and Friction Force Modelling

The model in consideration (Fig. 2) has outer race, inner race and rolling elements, whose positions are defined in an inertial reference frame (X-Y frame). The positions of centre of inner race, outer race, and ball with respect to inertial frame are designated as $O_1\left(x_i, y_i\right), O_2\left(x_o, y_o\right)$, and $C\left(x_b, y_b\right)$, respectively.

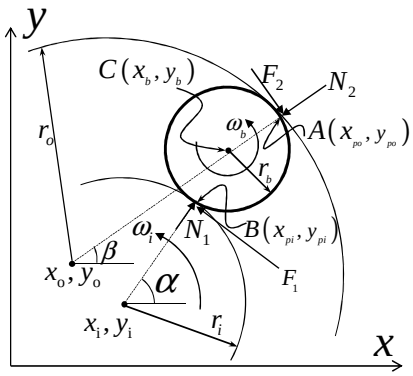

Fig.2. Contact forces in rolling element bearing.

The contact between inner race and *i*-th ball is at $B\left(x_{pi}, y_{pi}\right)$, and contact between outer race and ball is at $A\left(x_{po}, y_{po}\right)$. The radius of inner race, outer race and ball are $r_i = D_i/2, r_o = D_o/2$, and $r_b = d/2$, respectively, and the angle of rotation of outer race and inner race are β and α, respectively.

The positions of the contact points, neglecting the local deformations, can be defined as

$$\left.\begin{aligned} x_{pi} &= x_i + r_i\cos(\alpha) = x_b - r_b\sin(\alpha) \\ y_{pi} &= y_i + r_i\sin(\alpha) = y_b - r_b\cos(\alpha) \\ x_{po} &= x_o + r_o\cos(\beta) = x_b + r_b\cos(\beta) \\ y_{po} &= y_o + r_o\sin(\beta) = y_b + r_b\sin(\beta) \end{aligned}\right\} \quad (4)$$

The velocity at point B on the ball in tangential direction (V_t) and normal direction (V_n) can be written as

$$V_t = -\dot{x}_b\sin\alpha + \dot{y}_b\cos\alpha - \dot{\theta}_b r_b,\ V_n = \dot{x}_b\cos\alpha + \dot{y}_b\sin\alpha \quad (5)$$

where, $\dot{\theta}_b = \omega_b$ and angle $\alpha = \tan^{-1}\left(\left(y_b - y_i\right)/\left(x_b - x_i\right)\right)$. The same point's velocities on the inner race are given as

$$V_t = -\dot{x}_i\sin\alpha + \dot{y}_i\cos\alpha + \dot{\theta}_i r_i,\ V_n = \dot{x}_i\cos\alpha + \dot{y}_i\sin\alpha \quad (6)$$

The difference between the tangential velocities (slip) produces the friction. If there is no slip then there is pure rolling with no loss of energy. We assume lubricated bearing and thus viscous friction between the mating surfaces and by taking R_f as the effective viscous resistance,

$$\begin{aligned} F_t &= R_f\left(\dot{y}_i\cos\alpha - \dot{x}_i\sin\alpha + \dot{\theta}_i r_i - \left(\dot{y}_b\cos\alpha - \dot{x}_b\sin\alpha - \dot{\theta}_b r_b\right)\right) \\ &= R_f\left(\dot{x}_b - \dot{x}_i\right)\sin\alpha - R_f\left(\dot{y}_b - \dot{y}_i\right)\cos\alpha + R_f\left(\dot{\theta}_i r_i + \dot{\theta}_b r_b\right) \end{aligned} \quad (7)$$

Similarly, we can derive the equation for normal force contact point A and the normal and tangential force at point B. As two bodies having different radii of curvature in a pair of principal planes are in surface contact with each other, the force acting at the contact surface according to Hertzian contact theory [25] is given as

$$P = \begin{cases} K\delta^n & \text{for } \delta > 0 \\ 0 & \text{otherwise} \end{cases} \quad (8)$$

where P = roller/ball-raceway normal load, K = load deflection factor and n= load deflection exponent which is $3/2$ for ball bearing and $10/9$ for roller bearing.

The contact compression at the point of contact B depends on the position of the ball with respect to the centre of the inner race. So

$$\delta_i = r_i + r_b - \sqrt{(x_b - x_i)^2 + (y_b - y_i)^2} \tag{9}$$

Similarly, contact compression at contact point A is

$$\delta_o = r_b + \sqrt{(x_b - x_i)^2 + (y_b - y_i)^2} - r_o \tag{10}$$

where $r_o = r_i + 2r_b - \delta_p$ with δ_p being the rolling element pre-compression.

Note that the contact compression depends on the angular position of the rolling element, which is governed by the cage rotation, with the maximum deformation occurring in the load zone.

B. Modelling of Localized Faults

Faults are modelled using the principle presented in [16]. Outer race fault is modelled by taking a spall of depth C_d with an angular width of $\Delta\phi_d$. When a ball reaches a defined angular position ϕ_d, there is a sudden loss of contact as the ball enters the spall, and contact is regained instantly when it exits the spall. This gives a large amount of impulsive forces due to sharp changes in acceleration caused by sudden loss and gain of contact. The spall is modelled as a step function. In the case of the j^{th} ball, when $\phi_d < \phi_j < \phi_d + \Delta\phi_d$,

$$\delta_o = r_b + \sqrt{(x_b - x_i)^2 + (y_b - y_i)^2} - (r_o + C_d) \tag{11}$$

An inner race fault is modelled in similar fashion. It is defined as a spall of depth C_d and angular width of $\Delta\phi_d$. In this case, since the fault is on the inner race surface, it rotates with the same speed as that of inner race. Thus the value of ϕ_d depends on the angular rotation of the shaft.

$$\delta_i = (r_i + r_b - C_d) - \sqrt{(x_b - x_i)^2 + (y_b - y_i)^2} \tag{12}$$

In the case of ball/roller fault, the spall rotates at the same speed as the rolling element at ball spin frequency (BSF). The position of spall is defined as

$$\phi_s = \omega_{spin} t + \phi_0 \tag{13}$$

where ϕ_s is the position of spall and ϕ_0 is the initial starting location of spall.

The kinematic modelling considerations in [16] are not suitable in a dynamic modelling scenario with slip and radial as well as tangential movement of raceways and rolling elements. The inner race speed, cage speed and BSF may not be constant during dynamic loading, especially when the shaft is torque driven. Therefore, we adopt a separate geometric modelling scheme. The spall starting and ending positions on the element are tracked for this purpose.

For a fault on in the *j*-th rolling element, if the spall starts at point S1 and ends at point S2 then the positions of the spall beginning and end may be written as follows:

$$\left.\begin{aligned} x_{S1} &= \int_0^t \left(\dot{x}_b(\tau) - r_b \sin(\theta_b + \phi_{S1})\dot{\theta}_b(\tau)\right) d\tau \\ y_{S1} &= \int_0^t \left(\dot{y}_b(\tau) + r_b \cos(\theta_b + \phi_{S1})\dot{\theta}_b(\tau)\right) d\tau \\ x_{S2} &= \int_0^t \left(\dot{x}_b(\tau) - r_b \sin(\theta_b + \phi_{S2})\dot{\theta}_b(\tau)\right) d\tau \\ y_{S2} &= \int_0^t \left(\dot{y}_b(\tau) + r_b \cos(\theta_b + \phi_{S2})\dot{\theta}_b(\tau)\right) d\tau \end{aligned}\right\} \tag{14}$$

where $\theta_b = \int_0^t \dot{\theta}_b(\tau) d\tau$ is the angle rotated by the rolling element, and ϕ_{S1} and ϕ_{S2} are, respectively, the initial angular positions of the spall beginning and end with respect to the rolling element. The contact deformation at outer race contact is modelled by Eq. (11) when the line connecting the rolling element centre and the outer race centre lies within two lines connecting the outer race centre to the spall start and end positions and it also lies between two lines connecting the ball centre to the spall start and end positions. Otherwise, Eq. (10) is used. Likewise, contact with inner race considers a line connecting inner race centre to the rolling element centre and accordingly, one of Eqs. (9) and (12) is used to find the contact deformation. This modelling dynamically updates the contact in fault zones for any general motion of the raceways and rolling elements.

The contact with spalls in the outer and inner race are modelled in similar way by tracking the positions of spall start and end points and then considering that the suitable line connecting the rolling element centre to the raceway centre lies within the angle spanned by the spall start and end points. Note that one needs to use signed arctan function (generally referred to as atan2 function) for correct determination of spall contact.

Note that for rolling element fault, the loss of contact is detected twice for one revolution of the rolling element, *i.e.* once during contact with the inner race and another during contact with the outer race. As the curvatures of the inner and outer races are not the same, the values of angular widths of the fault $\Delta\phi_d$ are not same for both races. The depths to which the inner and outer races enter the spall are also affected by this curvature difference. The inner race will contact deeper and longer as compared to the outer race.

IV. BOND GRAPH MODEL

The bond graph model [26] of the bearing consists of four different sub-models, i.e., inner race, outer race, roller and cage. The entire system is modeled as a spring mass system (Fig. 3.) with the outer race of the bearing supported on a fixed platform through springs and dampers attached to it in X and Y directions. These springs and dampers model the structural stiffness and damping, including that of the bearing housing. Each rolling element is considered as a point mass which can be in contact with the inner race and outer race through two contact springs. The inner race is anchored to the inertial frame in X and Y direction through springs and dampers

which model the shaft bending stiffness and damping. The angular speed of the shaft is considered to be equal to that of inner race.

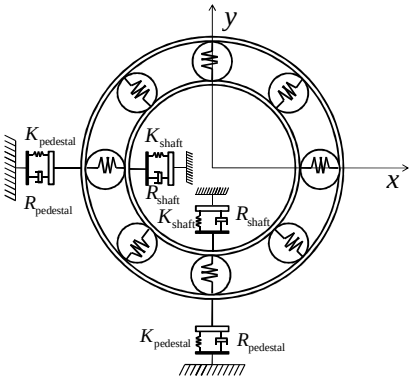

Fig. 3. Bearing as a multi-body system.

A. Inner race Submodel

The inner race is modeled as a spring mass system anchored to the inertial frame [16] as shown in Fig. 4. It is driven by a constant angular velocity source, *i.e.*, the velocity of the driven shaft $(\omega=\dot{\theta})$. It has three degrees of freedom.

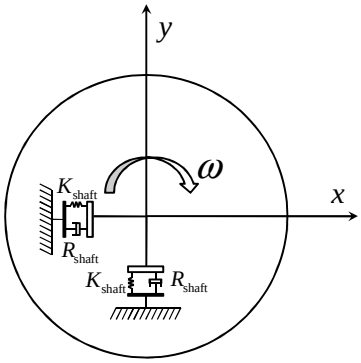

Fig. 4. Shaft model along with inner race.

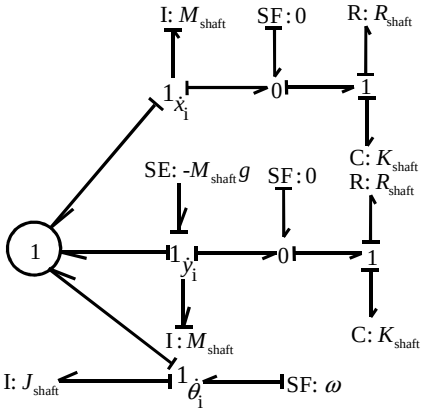

Fig. 5. Bond graph sub model of inner race and shaft.

Its bond graph is shown in Fig. 5 where element $\mathrm{I}: J_{\text{shaft}}$ models rotary inertia, two elements $\mathrm{I}: M_{\text{shaft}}$ model linear inertias in X and Y directions, two SF:0 elements model inertial frame anchoring, $\mathrm{SE}:-M_{\text{shaft}}g$ models self-weight with g as acceleration due to gravity, and $\mathrm{C}: K_{\text{shaft}}$ and $\mathrm{R}: R_{\text{shaft}}$ elements model the shaft bending stiffness and damping, respectively. The SF: ω element is replaced by a source of effort and a new R-element for bearing rotational damping is added to the corresponding junction to generate a torque driven model. This sub-model is interfaced to other sub-models through port 1 (shown within a circle). Here the interface port connects a set of bonds and thus, it is a vector bond port. This interface port will connect the inner-race sub-model to rolling element bearing sub-models.

B. Outer race Submodel

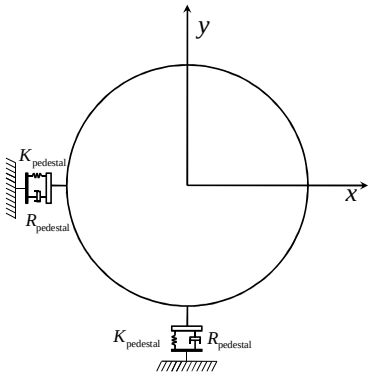

Fig. 6. Model of outer race with pedestal.

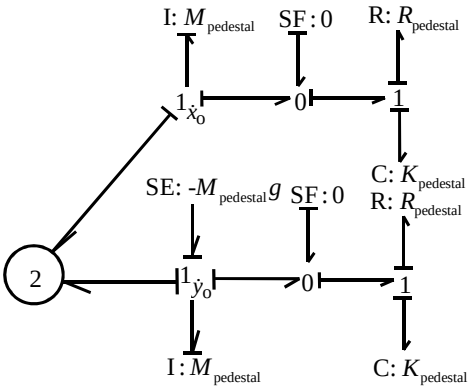

Fig. 7. Sub model of outer race using bond graph.

The outer race is fixed on the platform and it does not rotate. It can have translational motions along X and Y directions (Fig. 6). Its bond graph sub-model is shown in Fig. 7, where two $\mathrm{I}: M_{\text{pedestal}}$ elements model linear inertias of the bearing housing in X and Y directions, two $\mathrm{SF}: 0$ elements model inertial frame anchoring, $\mathrm{SE}:-M_{\text{pedestal}}g$ models self-weight, $\mathrm{C}: K_{\text{pedestal}}$ and $\mathrm{R}: R_{\text{pedestal}}$ elements model the structural stiffness and damping of the housing, respectively. This sub-model is interfaced to other sub-models, *i.e.*, the rolling element sub-models, through port 2 (shown within a circle).

C. Cage Submodel

The cage is modeled as a single rigid-body as shown in Fig. 8. Rollers or balls fit into the cage at various places. The contact with each rolling element is modeled in a separate sub-model. Therefore, two separate cage sub-models are created. The main cage model includes the

cage inertia whereas the additional cage sub-models are inertia-less models which simply model the contact with the rolling elements. The main cage sub-model is shown in Fig. 9 where element $\mathrm{I}: J_{\mathrm{cage}}$ models rotary inertia, two elements $\mathrm{I}: M_{\mathrm{cage}}$ model linear inertias in X and Y directions, and $\mathrm{SE}: -M_{\mathrm{cage}} g$ models self-weight.

This sub-model is interfaced to additional cage sub-models through port 4 (shown within a circle) and to rolling element sub-models through port 3 (shown within a circle).

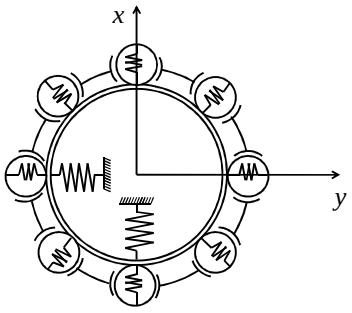

Fig.8. Cage model with ball.

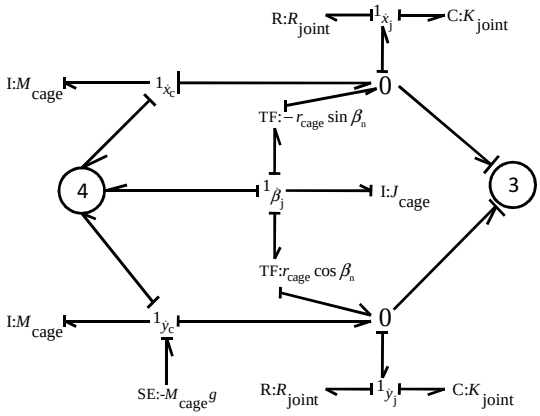

Fig.9. Sub-model of main cage.

Elements $\mathrm{C}: K_{\mathrm{joint}}$ and $\mathrm{R}: R_{\mathrm{joint}}$ model the contact stiffness and damping, respectively, between the cage and the rolling elements. It is assumed that the rolling elements (here rollers) are fixed to the cage through pin joints. The pin deformation transfers the force between the cage and the rolling element. Here, variable $r_{\mathrm{cage}} = D/2$ is the cage radius or pitch circle radius and β_n is the angular position of the *n*-th pin on the cage.

The additional cage sub-model is shown in Fig. 10. It is similar to the main cage sub-model, but inertias are missing. In this sub-model, ports 4 and 5 interface with main cage or other additional cage sub-models. In fact, the additional cage sub-model is coupled to the main-cage and other additional cage sub-models in such a way (See Fig. 11) that they share the same linear and rotary velocity (adjacent 1-junctions can be merged to single 1-junction). Note that each of these sub-models allows connection to one rolling element sub-model through port 3.

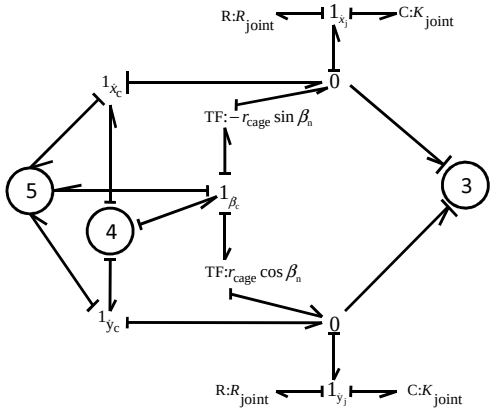

Fig.10. Additional cage sub-model.

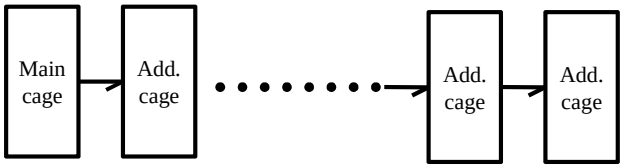

Fig.11. Word bond graph of cage.

D. Rolling Element Submodel

The rolling element is modelled as a point mass with two nonlinear contact stiffness and dampers as shown in Fig. 12. Here, ports 1 and 2 (shown within circles) connect to inner and outer race sub-models, respectively, and port 3 (shown within circle) connects to either main-cage or additional cage sub-model. Element $\mathrm{I}: J_{\mathrm{ball}}$ models rotary inertia, two elements $\mathrm{I}: M_{\mathrm{ball}}$ model linear inertias in X and Y directions, and $\mathrm{SE}: -M_{\mathrm{ball}} g$ models self-weight. The inner race is in contact is at point B and the outer race contact is at the point A as already shown in Fig. 2.

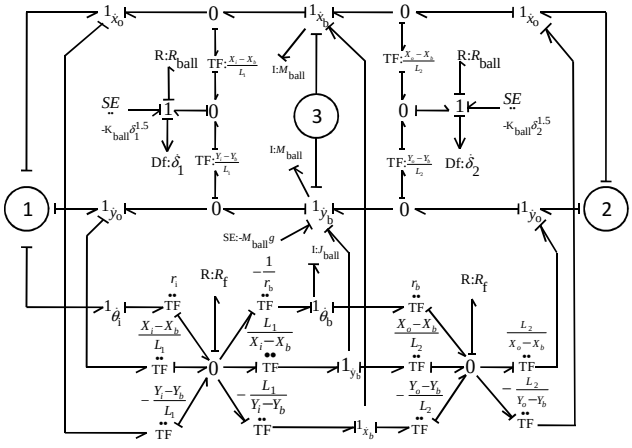

Fig.12. Bond Graph sub model of rolling element (Ball).

The non-linear contact forces along normal direction are modelled by two effort sources $\mathrm{SE}: -K_{\mathrm{ball}} \delta_1^{1.5}$ and $\mathrm{SE}: -K_{\mathrm{ball}} \delta_2^{1.5}$, where δ_1 and δ_2 are the deformations at the inner and outer race contacts, respectively. If there is loss of contact, *i.e.*, $\delta_i < 0, i \in 1,2$ then, the

corresponding source of effort is made zero. These contact deformations are obtained from measurements through flow detectors (Df elements). In addition, the contact damping is modelled through two R: R_{ball} elements. The roller model permits slip at the point of contact between the inner and outer races. The frictional force caused due to this slippage is a combination of viscous damping (due to the presence of lubricant) and Coulomb damping (due to metal on metal contact). In this sub model, the damping effect is mainly assumed to be viscous type and hence energy dissipation at the contact points is achieved using two viscous damping elements R: R_f. This damping generates the driving force to spin the rolling elements. If there is loss of contact then the value of R_f is switched from its nominal value to zero and vice versa, in a way similar to Eq. (8).

The various transformer elements used in the sub-model are used to compute the normal and tangential velocities as given by Eqns. (5), (6) and (7) for inner race contact and their extensions for outer race contact. The variables L_1 and L_2 represent the contemporary distance between the rolling element centre to the inner and outer race centres, respectively. The transformers used in upper part of the model are simply direction cosines used in Eqns. (5) and (6) (and their equivalent equations for outer race) whereas those in the lower half of the model are those appearing in Eq. (7) (and its equivalent form for outer race contact) to compute the slip between the rolling element and the raceways.

E. Integrated Model of Rolling Element Bearing

The complete bond graph model of the rolling element bearing is obtained by assembling the sub models into a form shown in Fig. 13. If there are n number of rolling elements then one needs that many rolling element sub-models, one main cage sub-model, n-1 numbers of additional cage sub-models, and one each inner and outer race sub-models.

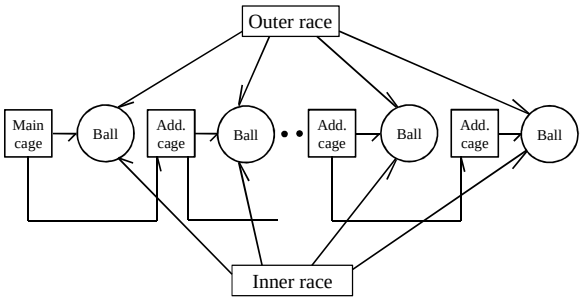

Fig.13. Word bond graph of rolling element bearing

V. SIMULATION RESULT

The bond graph model is simulated with the following geometric data: ball radius $r_{ball} = 0.2$ cm, pitch diameter $D = 3.4$ cm, fault depth $c_d = 1.0$ mm, fault angular width or span of 0.05 rad, number of balls N=8, ball pre-compression $\delta_p = 0.2$ μm and contact angle $\psi = 0$. The other parameters in the multi-body model of the bearing are given in Table I.

We simulate the following scenario of periodic shaft motion: the shaft rotates with angular speed 0.1047 rad/sec (1 RPM) for 24 s duration, stops rotating (dwells) for 5 s duration, reverses with angular speed of 1 RPM for 24 s duration and further stops (dwells) for 5 s duration. This cycle is then repeated. In this scenario, the shaft never completes one cycle of revolution. Moreover, the motion is oscillating, i.e., not in one direction, and the shaft angular speed is low. This specific scenario is inspired from the motions in the main shaft of a LD furnace bearing. Diagnosis of rolling element faults in such a scenario is a difficult task as will be shown in the next section.

TABLE I. MASS,STIFFNESS AND DAMPING OF BALL,PEDESTAL,CAGE WITH PIN AND SHAFT

Part	Mass (kg)	Stiffness(N/m)	Damping (Ns/m)
Ball	8.37×10^{-5}	9.92×10^{9}	1376.8
Pedestal with outer race	12.638	15.1×10^{6}	2210.7
Cage with pin	0.05	1×10^{5}	100
Shaft with inner race	6.2638	7.42×10^{8}	1376.8

The simulated force (proportional to acceleration) along y-direction in the pedestal and angle of inner race rotation vs. time for outer race, inner race and ball faults are shown in Figs. 14(a), 15(a) and 16(a), respectively. The reason for plotting the pedestal force in the y-direction is threefold: (1) usually, one measure accelerations using an accelerometer for fault diagnosis, (2) the pedestal is the most convenient place to mount the accelerometer, and (3) the rotor weight acts in y-direction and the fault signatures are large when measured in the load zone. The force signal is filtered through a band-pass filter placed around the bearing natural frequency. This removes noise in the signal, if any.

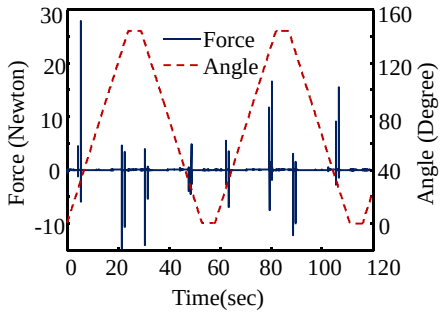

Fig.14(a). Simulated force in pedestal and angle of shaft rotation vs. time for outer race fault.

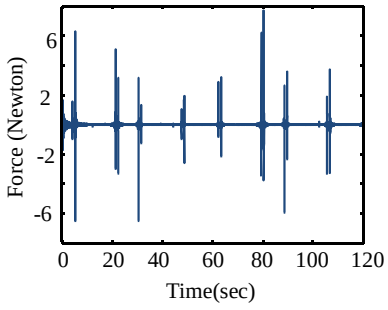

Fig.14 (b). Filtered signal for outer race fault.

The filtered signals corresponding to outer race, inner race and ball faults are shown in Figs. 14(b), 15(b) and 16(b), respectively. We can see distinct impacts when the raceway strikes a fault.

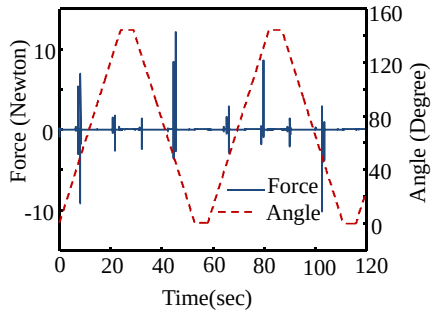

Fig.15 (a). Simulated force in pedestal and angle of shaft rotation vs. time for inner race fault.

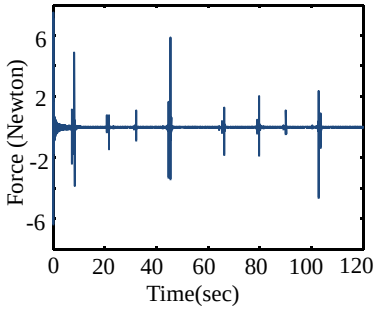

Fig.15(b). Filtered signal for inner race fault.

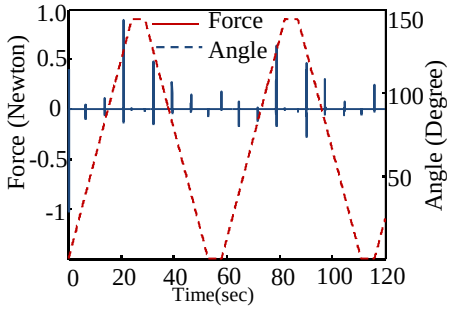

Fig.16 (a). Simulated force in pedestal and angle of shaft rotation vs. time for ball fault.

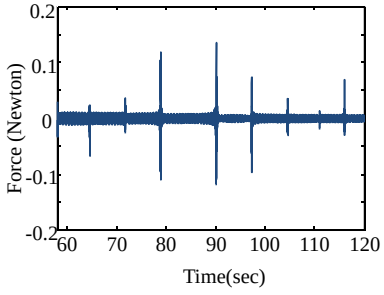

Fig.16 (b). Filtered signal for rolling element fault.

VI. Diagnosis of Rolling Element Bearing Fault in Unsteady Operation.

Note that usual frequency domain approaches (e.g., FFT or envelope spectrum) and time-frequency domain approaches (wavelet transform, etc.) cannot be applied when the inner race rotates at variable speed. For diagnosis of rolling element bearing faults during unsteady speed operation, one needs to measure the angle of rotation with time in addition to the vibration signal (acceleration or velocity of the pedestal). Then instead of performing a time or frequency domain analysis (in which fault transients become non-uniformly spaced) we can perform our analysis by using the angle of rotation in the place of time. Note that a fault is always encountered when the inner race rotates by a certain angle value irrespective of the speed at which it has been rotating.

Thus, instead of looking at the time interval between two adjacent hits, we can look at the angle turned between those two hits.

1) For outer race fault, on the average, $N(f_s)(1-d/D)/2$ *number of hits will occur for every 360 degree or one revolution for any general speed of rotation in one direction, i.e., hits will occur at intervals of* $720D/(N(D-d))$ *degrees.*

2) For inner race fault, $N(f_s)(1+d/D)/2$ *number of hits will occur for every 360 degree or one revolution. They will occur at somewhat smaller intervals as compared to outer race fault, i.e., at intervals of* $720D/(N(D+d))$ *degrees.*

3) For rolling element fault, the hits will occur at still smaller intervals of $360Dd/\left(D^2-d^2\right)$ *degrees.*

Thus, we will first collect angle turned vs. the vibration amplitude data. Then we can plot them in the form of a histogram (angle band *vs.* average vibration amplitude in that angle band). If it is found that there are distinct peaks in the histogram then, we can determine the intervals between the peaks and compare them to the fault characteristic angles defined in the above-mentioned three points.

Note that in this method of diagnosis, since the shaft rotates partially, it is possible that only impact at a specific angle is obtained.

In this case, histogram shows one peak which indicates some kind of fault. However, the type of the fault cannot be isolated. For fault isolation, two or more hits at different angles are required.

For the chosen bearing geometry, the angular intervals of hits for different types of faults are

Outer race fault = $720/\{N(D-d)\} = 102$ degree,

Inner race fault = $720/\{N(D+d)\} = 80.52$ degree,

and Ball fault = $360dD/\left(D^2-d^2\right) = 42.94$ degree.

The band-pass filtered force signal from outer race, inner race and rolling element fault simulations (See Figs. 14(b), 15(b) and 16(b), respectively) are plotted in histogram form with 1 degree angle bands in Figs. 17, 18 and 19, respectively.

In Fig. 17, two adjacent peaks occur at band numbers 27 and 33. The difference 6 degrees corresponds to the fault width, *i.e.*, the angle the inner race must turn so that a rolling element enters and exits from a spall. Likewise, the difference between adjacent peaks at bands 129 and 135 is also 6 degrees. The difference between the groups

of adjacent bands is $129 - 27 = 102$ degrees which is the fault characteristic angle for outer race fault. Thus, in a practical scenario, one can identify the fault from the peaks in the histogram.

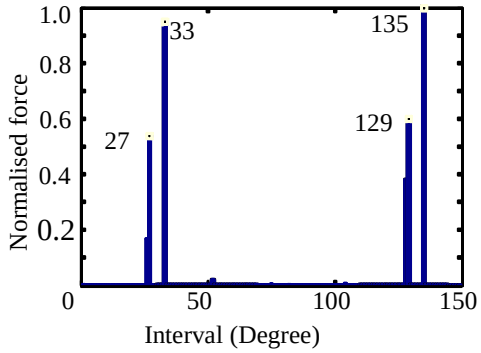

Fig.17. Normalised histogram for outer race fault.

The groups of adjacent peaks in the histogram plotted in Fig. 18 are spaced at interval of $126 - 45 = 81$ degrees. This matches with the fault characteristic frequency for inner race fault. Note that the amplitude levels in two groups of peaks are comparable for outer race fault whereas they are not so for both inner race and rolling element faults. This is because the hit for the latter two faults take place at different load zones. Also, the angle interval between the entry and exit into the spall on the inner race is smaller compared to that for the fault in the outer race.

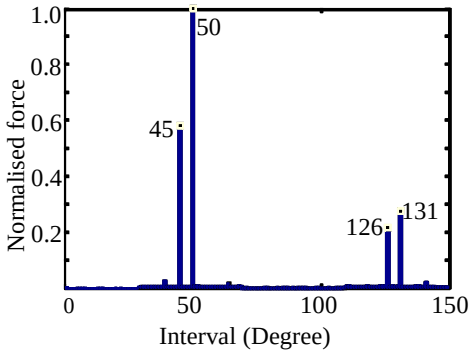

Fig.18. Normalised histogram for inner race fault.

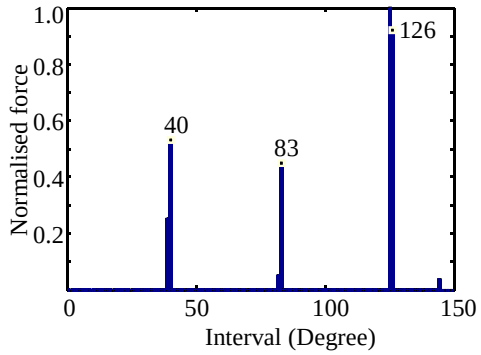

Fig.19. Normalised histogram for ball fault.

The histogram for rolling element fault (Fig.19) shows the gap between the groups of adjacent faults at intervals of $83 - 40 = 126 - 83 = 43$ degrees, which is the fault characteristic angle for the rolling element fault. Further to the variations in amplitude levels, one notices that the signals due to entry and exit from the spall are very closely spaced and indistinguishable. This is due to the high spinning speed of the rolling elements.

VII. CONCLUSION

In this paper, we have presented a multi-body dynamics bond graph model of rolling element bearing in presence of raceway and rolling element faults. The model considers nonlinear contact stiffness, contact friction, cage dynamics, and rolling element pre-compression. For high-speed rotation at constant speed in one direction, the simulated signal has the same basic characteristics as that of simulated and experimental signals reported in the literature [16]. However, the developed model is capable of simulating the response with variable speed/load operation such as that encountered in industrial applications.

Under variable speed/load/torque operation, usual frequency and time-frequency domain bearing fault diagnosis methods are not applicable. A set of new post-processing steps are thus proposed in which measurement of instantaneous angle and angular speed concurrently with the vibration amplitudes is desired. The proposed diagnosis framework has been explained in details and has been validated through simulated data.

The major contributions in the paper can be outlined at follows:

1) Development of a thorough multi-body dynamics model of the bearing with cage, roller, inner race and outer race, structural vibration, contact with impact and friction, etc. dynamics. The developed model can simulate both continuous and oscillating motions at unsteady speed.

2) The diagnosis scheme has been modified to used fault characteristic angles in place of fault characteristic frequencies. This approach decouples the rotor speed from the diagnosis requirement. However, one needs to measure the instantaneous angle of rotation in this approach. This approach is suitable to analyze faults during (a) unsteady speed rotation and (b) oscillating motion.

3) The developed diagnosis algorithm has been validated with simulated signals for various faults even when the simulated signal is willfully contaminated with Gaussian measurement noise.

REFERENCES

[1] C.M. Harris, A.G. Piersol, Shock and Vibration Handbook (Fifth ed.), McGraw-Hill, 2002.

[2] James I. Taylor, D. Wyndell Kirkland, The Bearing Analysis Handbook: a practical guide for solving vibration problems in bearings (First ed.), Vibration Consultants, 2004.

[3] M.S. Darlow, R.H. Badgley, and G.W. Hogg,"Application of High Frequency Resonance Technique for bearing diagnosis in helicopter gear boxes", US Army Air Mobility Research and Development Laboratory Report, USAAMRDL-TR, October 1974, pp.74-77.

[4] P.D. McFadden, J.D. Smith,"Vibration monitoring of rolling element bearing by the high-frequency resonance technique-a review", Tribology International, Vol. 17, Issue 1(1984), pp.3-10.

[5] J.E. Bambara, J.L. Frarey, R.L. Smith, " On-line acoustic detection of bearing defect", U.S. Patent 4,790,190. (1988).

[6] J. Antoni, R.B. Randall, "The spectral kurtosis: application to the vibratory surveillance and diagnostics of rotating machines", Mechanical Systems and Signal Processing, Vol. 20, Issue 2 (2006), pp.308-331.

[7] N. Sawalhi, R.B. Randall and H. Endo, "The enhancement of fault detection and diagnosis in rolling element bearing using minimum entropy de-convolution combined with spectral kurtosis", Mechanical Systems and Signal Processing ,Vol. 21, Issue 6 (2007),pp.2616-2633.

[8] H.M. Teager, "Some observations on oral air flow during phonation", IEEE Trans. Acoust., Speech and Signal Processing, Vol. 28, Issue 5 (1980), pp.599-601.

[9] P. Maragos, J.F. Kaiser and T.F. Quatieri, "On amplitude and frequency demodulation using energy operators", IEEE Transactions on Signal Processing, Vol. 41 (1993), pp.1532-1550.

[10] I.M. Howard, "Higher order spectral techniques for machine vibration condition monitoring", Proc. IMechE, Part G: Journal of Aerospace Engineering, Vol. 211(1997), pp. 211- 219.

[11] N.S. Swansson, S.C. Favaloro, "Application of vibration analysis to the condition monitoring of rolling element bearings", Aeronautical Research Laboratory, Propulsion Report 163, January 1984.

[12] J.M. Shea, J.K. Taylor, "Spike energy in fault analysis/ machine condition monitoring", Noise and Vibration Worldwide, February (1992), pp. 22-26.

[13] Prabhakar S., Mohanty A. R. and Sekhar A. S., "Application of discrete wavelet transform for detection of ball bearing race faults", Tribology International, Vol. 35, Issue 12 (2002), pp. 793-800.

[14] Dong Wang, Qiang Miao, Xianfeng Fan and Hong-Zhong Huang, "Rolling element bearing fault detection using an improved combination of Hilbert and Wavelet transforms", Journal of Mechanical Science and Technology, Vol. 23 (2009), pp. 3292-3301.

[15] P.K. Kankar, S.C. Sharma, S.P. Harsha, "Rolling element bearing fault diagnosis using wavelet transform", Neurocomputing, Volume 74, Issue 10 (2011), pp. 1638–1645.

[16] N. Sawalhi, R.B. Randall, "Simulating gear and bearing interactions in the presence of faults: Part I. The combined gear bearing dynamic model and the simulation of localized bearing faults", Mechanical Systems and Signal Processing, Vol. 22, Issue 8 (2008), pp. 1924-1951.

[17] P.D. McFadden, J.D. Smith, "Model for the Vibration Produced by a Single Defect in a Rolling Element Bearing", Journal of Sound and Vibration, Vol. 96 (1984), pp. 69-82.

[18] T.A. Harris, M.N. Kotzalas, Rolling Bearing Analysis: Essential Concept of Bearing Technology, Fifth edition, CRC press, New York, 2007.

[19] P.K. Gupta, "Dynamics of rolling element bearings part I-IV", Transactions of American Society of Mechanical Engineers, Journal of Lubrication Technology, Vol. 101 (1979), pp. 293-326.

[20] P.K. Gupta, Advanced dynamics of rolling element bearings, Springer Verlag, 1984.

[21] L.E. Stacke, D. Fritzson, P. Nordling, "BEAST - A Rolling Bearing Simulation Tool", Proc. IMechE, Part K: Journal of Multi-body Dynamics, Vol. 213(2) (1999), pp. 63-71.

[22] L.E Stacke, D. Fritzson, "Dynamic Behaviour of Rolling Bearings: Simulation and Experiments", Proc. IMechE, Part J: Journal of Engineering of Tribology, 2001, Vol. 215 (6), pp 499-508.

[23] A. Ashtekar, F. Sadeghi, L.E. Stacke, "A New Approach to Modeling Surface Defects in Bearing Dynamic Simulation", Journal of Tribology, Vol. 130(4) (2008), art. No. 041103.

[24] D. Fritzson, J. stahl, G. Morales-Espejel, "Simulation of fretting Fatigue in Conformal and Concentrated contacts", Tribology Online, 6(1) (2011), pp. 64-70.

[25] H. Hertz, "On the contact of rigid elastic solid and on hardness", in: Miscellaneous papers, MacMillan, 1896, pp. 163-183.

[26] A. Mukherjee, R. Karmakar, A.K. Samantaray, "Bond Graph in Modelling, Simulation and Fault Identification", CRC Press, 2006.